# Impact of magnetic fields on the stability of non-premixed flames

*A. Jocher*[1,2,3,*], *H. Pitsch*[1], *T. Gomez*[2,3], *J. Bonnety*[2,3], *G. Legros*[2,3]

[1]Institute for Combustion Technology, RWTH Aachen University, Aachen, Germany
[2]Sorbonne Univ, UPMC Univ Paris 06, UMR 7190, Inst Jean Le Rond dAlembert, F-75005, Paris, France
[3]CNRS, UMR 7190, Inst Jean Le Rond dAlembert, F-75005, Paris, France

**Abstract**

Mechanisms potentially driving the stabilization of an axis-symmetric sooting ethylene non-premixed flame are investigated. Established over the Santoro's burner, the flame burns into a co-flow consisting of 55% oxygen in volume and 45% carbon dioxide. While this flame naturally experiences flickering, recent experiments [1] showed that the oscillations vanish when the flame is exposed to a magnetic field. In the present work, a helium jet substitutes the fuel stream to reproduce the stabilization of the flame's plume. This configuration allows the influence of buoyancy, shear stress and magnetic body force to be assessed separately from the possible effect of soot radiation. The stabilization of the helium jet is experimentally evidenced and numerically reproduced.

## 1. Introduction

Combustion instabilities occurring in practical combustion systems can create conditions that may cause damage and mechanical failure. Conversely, these instabilities can also enhance mixing and burning rates [2]. The prediction of instabilities is therefore of high interest as it may enable their potential control.

Early studies of self-excited oscillations in buoyancy-dominated jet flames were conducted by Chamberlin and Rose [3]. Buckmaster and Peters [4] identified a modified Kelvin-Helmholtz-type buoyancy-driven instability as the origin of these oscillations. In numerical studies Davis et al. [5] and Ellzey and Oran [6] showed that the oscillations of jet diffusion flames are suppressed when gravity is reduced or set to zero.

In the work of Katta et al. [7], an oscillating methane flame was shown to become steady when 15 vol. % of acetylene were added and the volumetric flow rate of the mixture is kept constant. The increased soot formation due to doping and the associated increase in soot radiation were identified as the mechanisms driving the stabilization. Jocher et al. [8] recently showed that such an increase in soot formation may be induced by an increase of an upward gradient of the square of the magnetic flux density $\nabla(\mathbf{B}^2)$ in a steady laminar ethylene/air non-premixed flame.

Gilard et al. [9] studied the influence of a downward gradient $\nabla(\mathbf{B}^2)$ on the liftoff height of a co-flowing methane/air diffusion flame. The authors found that the magnetic force minimizes the liftoff height and increases the flow rate above which the flame blows out. Further stability investigations by Legros et al. [10] showed that an oscillation in a non-sooting methane flame was triggered by a downward gradient $\nabla(\mathbf{B}^2)$. The authors attributed these findings to the magnetic body force which may alternately strengthen buoyancy and shear stress, and in turn hastens the instability onset.

In Ref. 1, the influence of an upward static non-uniform magnetic field on the stability of an axis-symmetric sooting ethylene non-premixed flame was investigated. The co-flow consisted of 55% $O_2$ in volume and 45% $CO_2$. To expose this naturally oscillating flame to different $\nabla(\mathbf{B}^2)$, the axis-symmetric co-flow burner was located inside an electromagnet. It is experimentally observed that, without magnetic field influence, the self-induced flame flicker exhibits a frequency of about 12.5 Hz. At a gradient of the square of the magnetic flux density of 8.6 $T^2$/m, the oscillations are completely suppressed and a stable flame is observed.

In the present work, the mechanisms driving the stabilization of this flame experiencing a magnetic field are investigated. Experimental studies indicated that non-reactive, low-density jets flowing into higher density gases can sustain an absolute instability leading to periodic oscillations [11, 12, 13]. This oscillation phenomenon is found to be similar to the oscillations observed in diffusion flames. An important difference when comparing the unstable behavior of buoyant non-premixed flames to non-reacting jets is that in a flame, buoyancy is sustained due to hot combustion gases, while in a helium plume, the highest buoyancy influence is found close to the nozzle and decays downstream due to mixing with ambient fluid. To mimic the stabilization of the oscillating flame with the influence of buoyancy, shear stress and magnetic body force, a helium plume is studied here numerically. Similar Richardson numbers

* Corresponding author: a.jocher@itv.rwth-aachen.de

are used to obtain comparable buoyant conditions of the flame and the helium jet close to the nozzle exit. The computations are validated against index of refraction measurements with the Background Oriented Schlieren method (BOS) [14]. Changes in density fields, buoyancy and shear stress due to the magnetic field force are quantified. An unsteady helium jet is obtained computationally by increasing the Reynolds number. It can be observed that this unsteady helium jet is stabilized due to the influence of the magnetic field. The computations suggest that the alteration of buoyancy and shear stress is the governing process leading to the flame stabilization with the magnetic field.

## 2. Experimental configuration

A schematic of the experimental setup is provided in Fig. 1. The electromagnetic setup is described in detail in Refs. 8 and 10. For any current flowing through the coils of the electromagnet, the absolute $\nabla(\mathbf{B}^2)$ peak appears as a plateau, located at heights between $-140$ mm and $-110$ mm below the horizontal axis of symmetry of the electromagnet. The vertical component of $\nabla(\mathbf{B}^2)$ downstream the burner tip can be seen on the left hand side of Fig. 2. The magnitude of $\nabla(\mathbf{B}^2)$ is adjusted by a power supply that delivers a current up to 60 A flowing through the coils. This current generates a peak of the magnetic field's magnitude of 1 T at the core of the electromagnet together with a maximum $\nabla(\mathbf{B}^2)$ of 18.2 $T^2$/m within the aforementioned domain below the heart. The horizontal components of $\nabla(\mathbf{B}^2)$ were checked to be negligible. Therefore, the magnetic gradients' direction and the nozzle's vertical axis of symmetry are identical. The outlet of the helium tube is located in the region of maximum $\nabla(\mathbf{B}^2)$, i.e. -130 mm below the horizontal axis of symmetry of the electromagnet. The co-flow outlet is positioned -4 mm below the helium exit. In the following, the origin of the cylindrical coordinate system ($r$,$z$) is set to the center of the helium outlet.

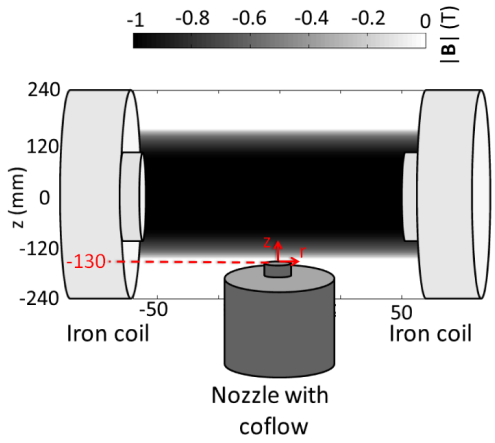


Figure 1: Schematic of the experimental setup. The electromagnet consists of two iron coils. The outlet of the helium tube is located -130 mm below the axis of symmetry of the electromagnet. The outlet of the co-flow is positioned -4 mm below the helium exit. A maximum magnetic field magnitude of 1 T can be generated, corresponding to a maximum $\nabla(\mathbf{B}^2)$ of 18.2 $T^2$/m.

The nozzle/co-flow setup corresponds to a Santoro type burner [15]. Helium is injected via a Bronkhorst EL-FLOW mass flow controller through a vertical axial brass nozzle. The diameter of the nozzle is 11.1 mm. The oxidizer consists of a mixture of $O_2$, diluted with $CO_2$. Two Bronkhorst EL-FLOW mass flow controllers enable the variation of the molar oxygen content $X_{O_2}$ in the co-flow. A final mixing of the co-flow is obtained in a concentric 102 mm inner diameter brass cylinder. A perforated brass plate, glass beads, and finally a 50 mm high ceramic honeycomb with a 1.2 mm cell-size straighten the co-flow.

To verify the implementation of the magnetic field body force terms, a numerical computation is compared to experimental measurements with Background Oriented Schlieren (BOS) technique. This technique is described in detail in Ref. 14. It allows the measurement of density gradients by ray deflection of a light source in the image plane. Here a 100 mW Spectra-Physics Excelsior Continuous Wave Laser operating at 405 nm (-5/+7 nm) is used as light source. Reference and acquisition pictures are taken continuously of a round background image with black and white dot patterns. Then, the images are processed with a commercial adaptive cross correlation algorithm from Dantec Dynamic Studios to obtain fields of index of refraction gradients that are qualitatively compared to the computed density gradients.

## 3. Computational set-up

To reproduce the experimental observations computationally, 2D axis-symmetric numerical simulations are carried out using the CIAO in-house code. The numerical methods of the code are described in Ref. 16. It solves the Navier-Stokes equations in the low Mach number limit, using a parallel second order, semi-implicit, finite difference method with Crank-Nicolson type time stepping and an iterative predictor-corrector updating scheme. Spatial and temporal staggering is used to increase the accuracy of stencils. The Poisson equation for the pressure is solved by the multi-grid HYPRE solver. Momentum equations are spatially discretized with a second order scheme. Scalar equations are discretized with a third order WENO scheme [17]. Further details about the applied numerical algorithm and code verification including a momentum-driven helium/air jet can be found in Ref. 16.

The flow is treated as a multi-component mixture. Viscosity, thermal conductivity and the species diffusion coefficients are computed with the approximate expressions prescribed by Law et al. [18]. Species diffusion due to the magnetic field force is included, while diffusion due to pressure gradients, heating due to viscous dissipation, as well as second-order processes known as Soret and Dufour effects are neglected.

Constant Lewis numbers for the transported species were pre-computed with FlameMaster [19], using 1D counterflow conditions. The obtained values are shown in Table 1.

| | He | $O_2$ | $N_2$ | $CO_2$ |
|---|---|---|---|---|
| Le | 0.286 | 0.986 | 1.004 | 1.114 |

Table 1: Constant Lewis numbers for transported species.

The code is extended with terms modeling the magnetic body force to account for the magnetic field influence. The approach of Yamada et al. [20] and Shinoda et al. [21] is used. These authors stated that the magnetic force $F_i$ per unit volume acting on chemical species $i$ can be defined as:

$$\mathbf{F}_i = \frac{1}{2\mu_0}\rho Y_i \chi_i \nabla(\mathbf{B}^2), \tag{1}$$

where $\mu_0$ is the magnetic permeability of vacuum, $Y_i$ the mass fraction of species $i$, and $\chi_i$ its magnetic susceptibility per unit mass. The latter quantity is given by Curie's law as:

$$\chi_i = \frac{N_A g_L^2 \mu_B^2 S_i(S_i+1)\mu_0}{3kTm_i}. \tag{2}$$

$N_A, g_L, \mu_B$ and $\mu_0$ are the Avogadro number, the Lande's g-factor, the Bohr magneton, and the magnetic permeability of vacuum, respectively. $k$ is the Boltzmann constant, $T$ the temperature, and $m_i$ the molar mass of species $i$. $S_i$ is the total angular momentum of electron spin of species $i$ [21]. Species with no unpaired electron are diamagnetic. Species with one or more unpaired electrons are paramagnetic, exhibiting a relatively large positive value of $\chi_i$ [21]. Within the framework of the present study, only $O_2$ is paramagnetic due to its two unpaired electrons. Therefore $S_{O_2}$ = 1. He, $N_2$ and $CO_2$ have no unpaired electrons. As a result, their $S_i$ values are set to zero.

The body force term $F_i$ is added to the momentum equation, the species, and energy equation in the governing equations. The Lorentz force for ionic species is assumed negligible due to the absence of ionizable substances like alkali elements. In a laminar jet flame, Legros et al. [10] experimentally evidenced that the Lorentz force can be neglected due to the slow velocities of the potential ions produced along the chemical pathways.

A schematic of the computational domain is shown in Fig. 2. Matching the experimental setup, helium is injected through a 14 mm long nozzle into the computational domain. The nozzle's wall is 0.8 mm wide and its inner radius is 5.55 mm. The helium jet is surrounded by a co-flowing stream consisting of oxygen and carbon dioxide, as in the experiment. The co-flow is injected via a 10 mm long tube into the computational domain. This tube has a wall thickness of 5 mm and an inner radius of 51 mm. Both inflows are modeled as uniform plug flows, with a helium velocity of injection ranging from 20.5 cm/s to 5 m/s and a constant co-flow velocity of 15.3 cm/s. The overall extension of the domain is 0.5 m and 1.2 m in the radial and axial directions, respectively. This allows the effect of the surrounding quiescent air to be captured.

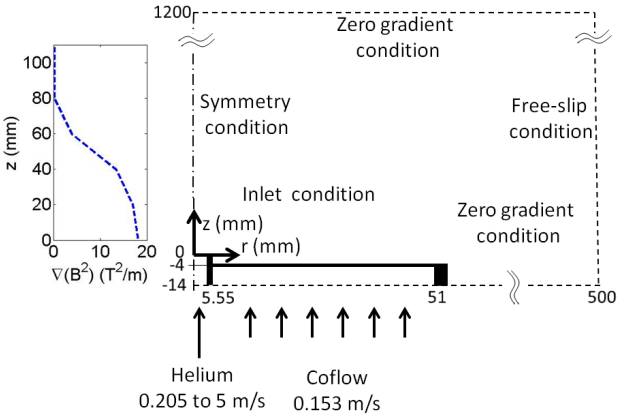


Figure 2: On the left, evolution of $\nabla(\mathbf{B}^2)$ z-component along the axis of symmetry. On the right, schematic of the computational domain for the simulation of the helium/co-flow jets surrounded by quiescent air.

The vertical boundary on the right hand side of the domain follows a free-slip condition. The top boundary is designed as an outflow with zero gradient conditions, as well as the area of quiescent air around the co-flow tube. On the centerline, symmetry conditions are applied as the flow is expected to be axis-symmetric. The numerical simulation is carried out on a non-uniform two-dimensional cylindrical mesh with 276 (z) x 156 (r) control volumes. The grid is refined at the vicinity of the helium outlet section, with a maximum resolution of 0.2 mm in radial and axial directions.

On the left hand side of Fig. 2, the experimental measurements of the $\nabla(\mathbf{B}^2)$ z-component along the axis of symmetry are shown. A Gauss meter enables these measurements. Its maximum value is located close to the nozzle outlet section. The magnitude of $\nabla(\mathbf{B}^2)$ then decays downstream. A 1D function is shown to decently fit this evolution and is then implemented into CIAO. The function is imposed in the simulations for the cases with magnetic field influence.

## 4. Results and discussion

### *4.1. Constants and parameters*

The following study is conducted at atmospheric pressure and constant ambient temperature of 300 K. Helium is chosen to reproduce the low density flow of hot combustion gases. This configuration allows buoyancy and shear stress to act on the helium jet and to produce in certain conditions flow instabilities. The influence of soot radiation on the onset of these instabilities will not be modeled. Potential stabilization of the helium jet due to magnetic body force is investigated.

The co-flow is a mixture of 55 vol. % oxygen and 45% carbon dioxide. A high oxygen content is chosen as oxygen is highly susceptible to the magnetic force. In this way, the impact of the magnetic field is expected to be emphasized. The co-flow is complemented by $CO_2$ as

the corresponding ethylene flame exhibits a natural oscillation while it is stable when $N_2$ substitutes $CO_2$. The co-flow volumetric flow rate is kept constant at 1233 $cm^3/s$ corresponding to an inflow velocity of 15.3 cm/s. For the code validation a laminar helium plume is chosen with a volumetric flow rate of 20 $cm^3/s$ corresponding to a velocity of 20.5 cm/s at the helium outlet section and a Reynolds number of 19.2. This configuration is also used to study computationally the magnetic field impact. To investigate the stability behavior, an unsteady helium jet is then obtained computationally by increasing the helium inflow velocity to 5 m/s, i.e. the Reynolds number to 469. It can be observed that this unsteady helium jet is stabilized with a maximum $\nabla(\mathbf{B}^2)$ of 18.2 $T^2/m$.

### 4.2. *Computational model validation*

To validate the implementation of the magnetic body force terms, numerical computations are compared to Background Oriented Schlieren (BOS) measurements. The deflection angles due to density gradients, obtained with BOS, are shown on the left hand side of Fig. 3. The helium and co-flow velocities are 20.5 cm/s and 15.3 cm/s, respectively. On the right hand side of Fig. 3, the corresponding numerical computations are shown. The deflection angle is computed to compare qualitatively the computational to the experimental results. Starting from the computed density, the index of refraction field $n$ is calculated with the Gladstone-Dale equation [22]: $n = 1 + \rho R_G$. $R_G$ is the Gladstone-Dale constant, a molecular property, slightly depending on the light-source wavelength. For fluid mixtures $R_G$ is the sum of the mole fraction and the Gladstone-Dale constant of all included species $i$: $R_G = \sum_{i=1}^{S}(R_{Gi}X_i)$. The $R_{Gi}$ values for He, $O_2$, $N_2$ and $CO_2$ are computed from Gardiner et al. [22] for a wavelength of 405 nm. Next the gradients in r- and z-direction for $n$ are calculated before integrating them along the line-of-sight to obtain the deflection angles of the projected data. The calculated projected deflection angles are compared to the measured deflection angles.

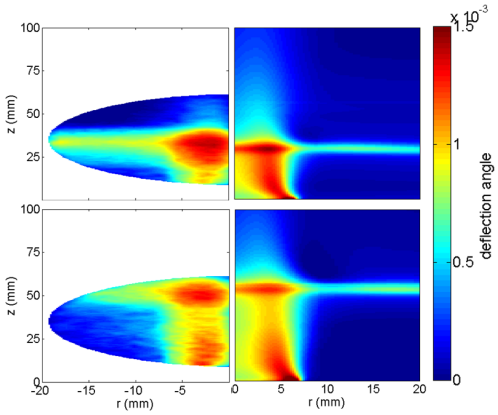


Figure 3: Comparison between the measured deflection angles on the left and the computed angles on the right. Upper row: without magnetic field influence. Lower row: $\nabla(\mathbf{B}^2)$ set to 18.2 $T^2/m$.

The upper row of Fig. 3 shows the experimental and numerical angles without magnetic field influence. A horizontal beam of higher magnitude appears in both the experiment and the computation around 30 mm above the helium outlet section. This beam indicates a density gradient resulting from the transition of the co-flow mixture to the surrounding air. The red vertical section close to the axis of symmetry indicates the density gradient from the lighter helium plume to the heavier co-flow. With the maximum $\nabla(\mathbf{B}^2)$ of 18.2 $T^2/m$, the horizontal beams in both the experimental and numerical fields are shifted downstream and it appears in the computation at about 60 mm. This region was only partly accessed experimentally with the current setup. However it indicates that the co-flow is extended upstream as evidenced by the computational fields.

### 4.3. *Magnetic field impact on laminar jets*

Figure 4 illustrates the co-flow downstream shift mentioned in the previous section. Dark blue areas in the center are mainly composed of helium as the density of pure helium is 0.17 $kg/m^3$. The surrounding deep red areas represent the co-flow mixture whose density is 1.67 $kg/m^3$. As in the experiment, the co-flow is surrounded by quiescent air on both sides (not shown here), as well as above the co-flow mixture ($z > 30$ mm). The density of air is indicated by orange areas with a density of 1.2 $kg/m^3$. This subdivision of the domain is generated by the chosen co-flow velocity and density. The co-flow mixture is heavier than the surrounding air but is injected upward. This exit velocity is slowed down and the co-flow mixture diverges into the quiescent air around the co-flow. Therefore a maximum co-flow vertical extension of 30 mm is obtained like in the experiment. Figure 4(b) shows that this vertical extension is increased to about 60 mm under the influence of the magnetic field gradient. To explain this effect, it is important to clarify that $O_2$ is the only paramagnetic species in this configuration, therefore the only species susceptible to the magnetic field influence. Oxygen is found in 55 vol. % in the co-flow. The second important parameter is the evolution of $\nabla(\mathbf{B}^2)$. It decreases from its maximum value of 18.2 $T^2/m$ at the helium outlet section to zero 80 mm downstream.

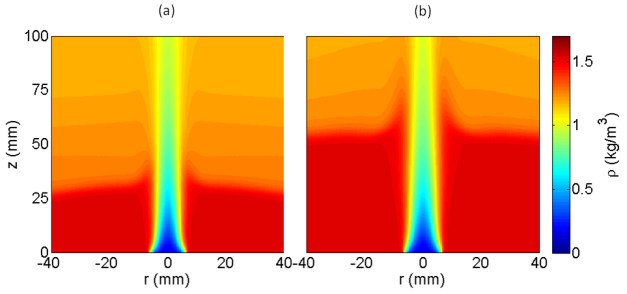


Figure 4: Computed density distribution. Helium velocity 20.5 cm/s, co-flow velocity 15.3 cm/s: (a) without magnetic field influence; (b) $\nabla(\mathbf{B}^2)$ set to 18.2 $T^2/m$.

Both parameters mainly influence the magnetic field body force.

In Fig. 5, the z-component of the overall body force in the momentum equation is shown, without any magnetic field influence on the left, and with the magnetic body force induced when $\nabla(\mathbf{B}^2)$ is set to 18.2 $T^2$/m on the right. In Fig. 5(a), the body force term only includes the gravity contribution $\rho\mathbf{g}$, $\mathbf{g}$ being the acceleration due to gravity. A negative value of -14 N/$m^3$ is seen for the heavy co-flow. In Fig. 5(b) the body force is the addition of the gravity contribution and the magnetic body force applied to $O_2$: $\rho\mathbf{g} + \mathbf{F}_{O_2}$. Thus, the distribution of the overall body force has been significantly affected by the magnetic field. Here, for the region exhibiting high $Y_{O_2}$ together with high $\nabla(\mathbf{B}^2)$, a reduced body force of -9 N/$m^3$ is observed. Therefore, the influence of gravity in this region is considerably weakened by the magnetic field. As a result, the deceleration of the co-flow mixture is reduced as compared to the configuration without any magnetic field and the co-flow can further penetrate the quiescent air.

Besides the magnetic influence on the momentum equation, the magnetic effect on the species distribution needs to be evaluated. To assess the importance of species diffusion due to $\nabla(\mathbf{B}^2)$, the diffusion velocity $\mathbf{V}_{O2}^{Conc}$ due to the concentration gradient of $O_2$ has to be evaluated using a formulation that includes the magnetic field influence. The diffusion velocity $\mathbf{V}_{O2}^{Conc}$ is defined as follows:

$$\mathbf{V}_{O2}^{Conc} = -\frac{D_{O_2}}{X_{O_2}} \nabla X_{O_2} \tag{3}$$

The diffusion velocity $\mathbf{V}_{O2}^{MagF}$ due to magnetic influence is the result of the discrepancies among the body forces acting on the different species that $\nabla(\mathbf{B}^2)$ generates:

$$\mathbf{V}_{O2}^{MagF} = \frac{D_{O_2}}{X_{O_2}} \frac{\rho}{p} \frac{1}{2\mu_0} \nabla(\mathbf{B}^2) Y_{O_2} \sum_{j=1}^{N} [Y_j(\chi_{O_2} - \chi_j)]. \tag{4}$$

It is found that the diffusion velocity due to the magnetic influence is six orders of magnitude smaller than the diffusion velocity due to concentration gradients, negligible and therefore not shown.

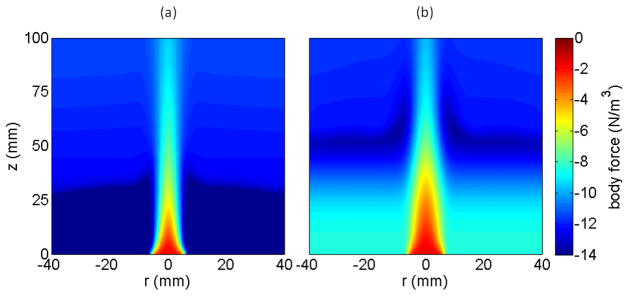


Figure 5: Computed body force distribution. (a) Gravity without magnetic force. (b) Sum of gravity and magnetic force for $\nabla(\mathbf{B}^2)$ set to 18.2 $T^2$/m.

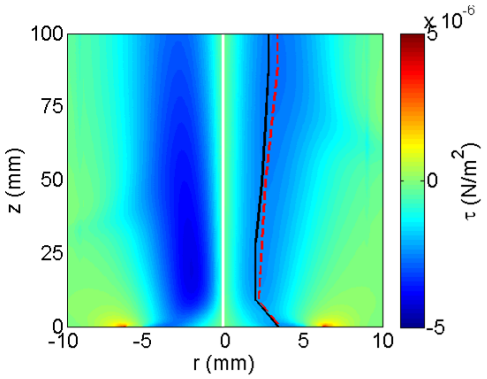


Figure 6: Comparison of shear stress distribution without magnetic field (left half) and for $\nabla(\mathbf{B}^2)$ set to 18.2 $T^2$/m (right half). The field on the left half has been multiplied by -1 to be shown on the same color scale. The black solid line and the red dashed one indicate the radial locations of the minimum shear stress along the vertical axis without any magnetic field and for $\nabla(\mathbf{B}^2)$ set to 18.2 $T^2$/m, respectively.

Buckmaster and Peters [4] identified flame oscillations as a modified Kelvin-Helmholtz-type buoyancy-driven instability, due to gravitational acceleration and the thermomechanical properties of hot and cold gas. For this reason, the change in shear stress due to the magnetic field is illustrated in Fig. 6. The shear stress $\tau$ is computed as $\mu\frac{\partial u}{\partial r}$, $\mu$ being the dynamic viscosity and $\frac{\partial u}{\partial r}$ the radial component of the gradient of the stream-wise velocity $u$. On the left half of Fig. 6 the shear stress distribution without any magnetic influence is shown. Its minimum value of $\tau$ = -4.5e$^{-3}$ N/$m^2$ is located between 10 and 35 mm above the nozzle exit and 2 mm in the radial direction. Further downstream, the shear stress decreases. When $\nabla(\mathbf{B}^2)$ is set to 18.2 $T^2$/m, the minimum shear stress is increased to -2.2e$^{-3}$ N/$m^2$ beginning at z = 65 mm above the nozzle. Overall, a thinner shear stress distribution in the lower domain can be observed under the magnetic influence. The minimum shear stress value is increased and the location of the minimum shear stress is moved radially outward with the magnetic field.

### 4.4. *Stabilization of a self-excited oscillating jet via magnetic field*

Based on the former findings the influence of the magnetic field on jet stability is investigated. The helium inflow velocity is therefore increased to 5 m/s corresponding to a Reynolds number of 469. In Fig. 7(a), the density distribution without magnetic influence is shown. As for the configuration with $v_{He}$ = 20.5 cm/s, the co-flow penetrates up to $z$ = 25 mm. However, the central region exhibits now a vortex-like structure with axis-symmetric perturbations. This structure vanishes under the magnetic influence shown in Fig. 7(b). A possible explanation is the change in shear stress due to magnetic field influence shown in Fig. 6. While this finding now needs further investigations, it can be speculated that under the magnetic influence the radial component of the gradient of the stream-wise velocity is smoothed.

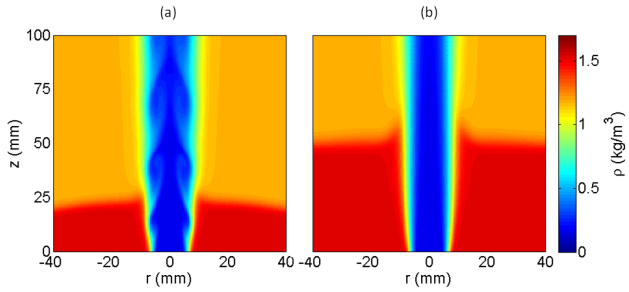


Figure 7: Computed density distribution. Helium velocity 5 m/s, co-flow velocity 15.3 m/s: (a) instantaneous field without magnetic influence; (b) $\nabla(\mathbf{B}^2)$ set to 18.2 $T^2$/m.

This weakens the generation of vorticity generation, thus reduces the flow disturbance. Finally, without the perturbations of the helium jet, the mixing between helium and its surrounding is reduced.

## 5. Conclusion

In this study a new mechanism for altering buoyant jet behavior without the need of altered gravity environment like in drop towers, parabolic flights, or low gravity environments was assessed. A helium jet that generates vortex-like structures is used to mimic the behavior of a flame's plume. Just like for the flame, the helium jet stabilization can be driven by a gradient of the magnetic flux density. The use of the helium jet allows the effects of buoyancy, shear stress, and magnetic body force to be reproduced, while the role of soot radiation on the flame stability are not included. The helium jet could be computationally stabilized under the influence of the magnetic gradient. Reduction of the maximum shear stress magnitude and changes in the shear stress distribution have been quantified and identified as a possible phenomenon leading to the stabilization with the magnetic field. The velocity gradient reduction was shown to result from a reduced buoyancy. Indeed, the magnetic body force is opposed to the gravitational force. Consequently, with magnetic field, buoyancy is reduced especially close to the helium outlet section, which extends the co-flow penetration in the stream-wise direction.

## Acknowledgements

This work was performed using HPC resources from GENCI-CINES (Grant 2014 - C 201 32 B 7144). It was financially supported by Université franco-allemande/Deutsch-Französische Hochschule. The authors feel grateful to H. Dutilleul and J.M. Citerne for their technical support.

## References

[1] A. Jocher, H. Pitsch, T. Gomez, J. Bonnety, G. Legros, Stabilization of sooting non-premixed flames via magnetic field, -. In preparation.

[2] M. Matalon, Annu. Rev. Fluid Mech. 39 (2007) 163–191.

[3] D. S. Chamberlin, A. Rose, Engineering Chemistry 20 (1928) 1013–1016.

[4] J. Buckmaster, N. Peters, Symp. (Intl.) Combust. 21 (1988) 1829 – 1836.

[5] R. Davis, E. Moore, W. Roquemore, L.-D. Chen, V. Vilimpoc, L. Goss, Combust. Flame 83 (1991) 263 – 270.

[6] J. Ellzey, E. Oran, Symp. (Intl.) Combust. 23 (1991) 1635 – 1640.

[7] V. R. Katta, W. M. Roquemore, A. Menon, S.-Y. Lee, R. J. Santoro, T. A. Litzinger, Proc. Combust. Inst. 32 (2009) 1343 – 1350.

[8] A. Jocher, H. Pitsch, T. Gomez, G. Legros, Proc. Combust. Inst. 35 (2015) 889–895.

[9] V. Gilard, P. Gillon, J.-N. Blanchard, B. Sarh, Combust. Sci. Technol. 180 (2008) 1920–1935.

[10] G. Legros, T. Gomez, M. Fessard, T. Gouache, T. Ader, P. Guibert, P. Sagaut, J. Torero, Proc. Combust. Inst. 33 (2011) 1095 – 1103.

[11] P. Monkewitz, D. Bechert, B. Barsikow, B. Lehmann, J. Fluid Mech. 213 (1990) 611–639.

[12] D. Kyle, K. Sreenivasan, J. Fluid Mech. 249 (1993) 619–664.

[13] B. M. Cetegen, K. D. Kasper, Phys. Fluids 8 (1996) 2974–2984.

[14] A. Jocher, H. Pitsch, T. Gomez, J. Bonnety, G. Legros, Near field characteristics of low density jets, exposed to magnetic fields, -. In preparation.

[15] R. Santoro, H. Semerjian, R. Dobbins, Combust. Flame 51 (1983) 203 – 218.

[16] O. Desjardins, G. Blanquart, G. Balarac, H. Pitsch, J. Comput. Phys. 227 (2008) 7125–7159.

[17] G.-S. Jiang, C.-W. Shu, J. Comput. Phys. 126 (1996) 202–228.

[18] C. K. Law, Combustion Physics, Cambridge University Press, 2006. Cambridge Books Online.

[19] H. Pitsch, Flamemaster., -. A C++ computer program for 0D combusiton and 1D laminar flame calculations.

[20] E. Yamada, M. Shinoda, H. Yamashita, K. Kitagawa, Combust. Flame 135 (2003) 365 – 379.

[21] M. Shinoda, E. Yamada, T. Kajimoto, H. Yamashita, K. Kitagawa, Proc. Combust. Inst. 30 (2005) 277 – 284.

[22] W. G. Jr., Y. Hidaka, T. Tanzawa, Combust. Flame 40 (1981) 213 – 219.